LARGE SYNOPTIC SURVEY TELESCOPE

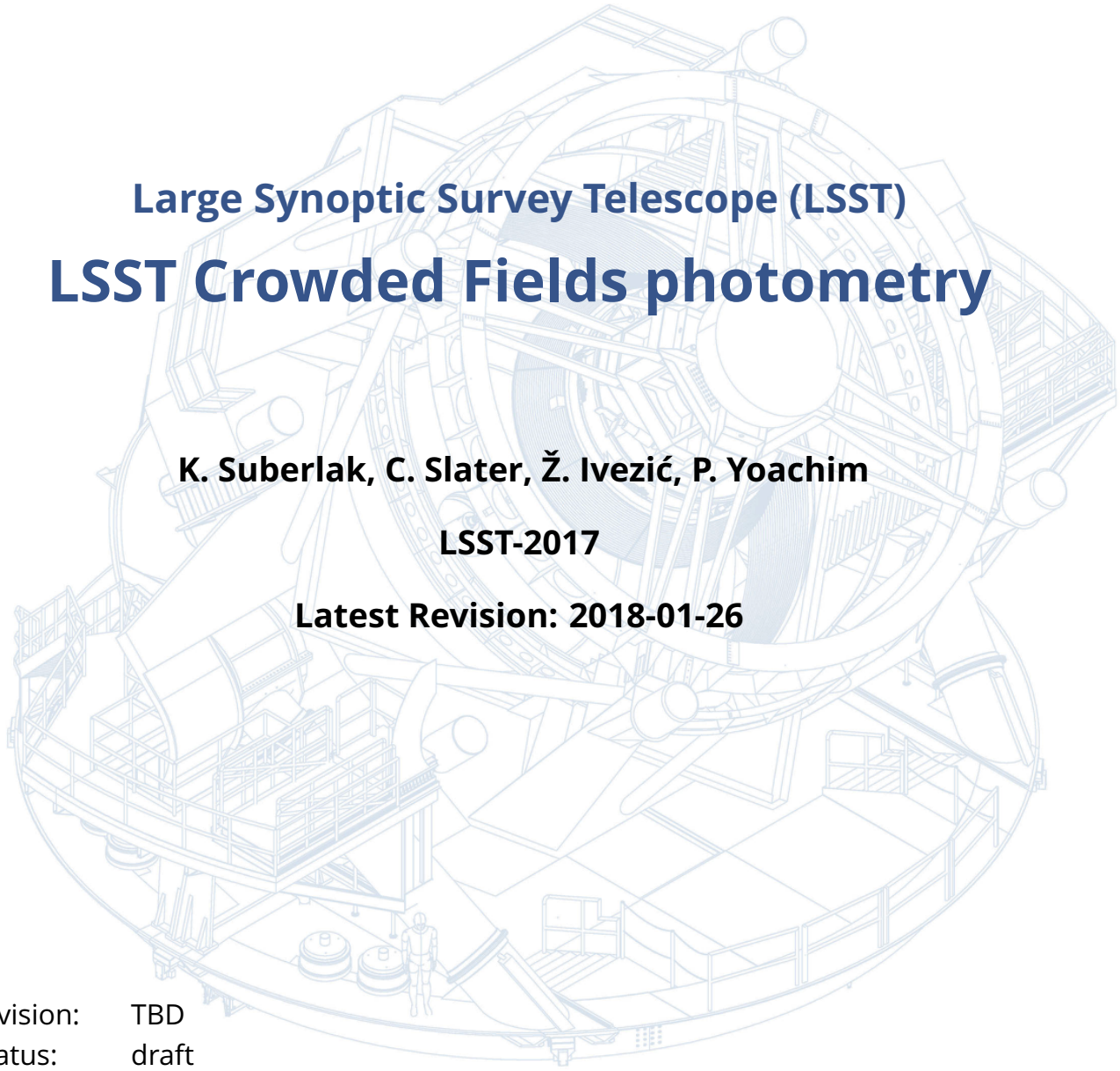

Large Synoptic Survey Telescope (LSST)

LSST Crowded Fields photometry

K. Suberlak, C. Slater, Ž. Ivezić, P. Yoachim

LSST-2017

Latest Revision: 2018-01-26

revision: TBD
status: draft

Abstract

A report on the performance of current LSST Stack pipelines in crowded stellar fields. Using the real data we explore the metrics that could be used to direct decision-making process for pipeline improvements. The quality metrics show also a way to validate the performance of LSST pipelines after major software upgrades.

Change Record

Version	Date	Description	Owner name
1	2017-07-16	First draft.	Krzysztof Suberlak
2	2017-10-19	Updated outline.	Krzysztof Suberlak
2	2018-01-25	Major revision.	Krzysztof Suberlak

Contents

1 Introduction

We report on the performance of the Large Scale Synoptic Telescope (LSST) science pipelines [1], also known as 'the LSST stack', in stellar fields of varying levels of crowdedness.

The LSST will sample every night over 1,000 regions in the sky , delivering terabytes of raw data in need of processing: photometric and astrometric calibration, to deliver a calibrated exposure image, as well as a source catalog, among other image products[2] [3].

The survey sky is composed of regions very diverse in terms of stellar density, or crowdedness: from high density low-galactic latitude regions that have tens of millions of sources per square degree, to low-density regions towards the galactic poles with less than thousand sources per square degree.

Deblending and successful photometry is an inherent part of any astronomical data processing pipeline. There exists a body of research answering questions that are specific to crowded stellar fields, eg. how many beams do we need per source (see [2]), or how the crowded fields photometry can be approached in the era of large telescopes [4] Other studies involved eg. HyperSuprime CAM pipeline (developed in parallel with the LSST Stack), recognizing that the deeper the survey, the higher the stellar densities encountered, and the onset of blurring the the boundaries between deblending, measurement, and detection [1].

In this report we compare the 'out-of-the-box' LSST Stack tools, in particular processCcd.py, to the DECAm [Galactic] Plane Survey (DECAPS) catalogs based on the NOAO state-of-the-art community pipeline ([5]). First we use the LSST Metrics Analysis Framework Galfast simulation of the night sky find regions representing various stellar densities - see Sec. 2. Then we query the DECAPS image database for images that were taken at exposures and filters that reach similar depth to the LSST single-visit depth (Sec. 3). We select few DECAPS exposures at each density level, and process with LSST Stack tools (Sec. **??**). In Sec. **??** we compare the results of LSST processing and the DECAPS single-epoch catalogs, and develop the quality metrics. Finally in Sec. **??** we make recommendations for future work.

[1] https://pipelines.lsst.io
[2] http://ls.st/LSE-163

2 Identifying density regions

To identify regions representing different stellar densities we use the LSST Metrics Analysis Framework [3] simulated stellar density map prepared by P. Yoachim and L. Jones [4]

The resulting dataset `starDensity_r_nside_64.npz` contains 64 magnitude bins, with the entire sky divided into 49152 healpixels [5]. Each healpixel contains information about the number of stars per square degree in a given magnitude bin in the simulated sky - see Fig. 1.

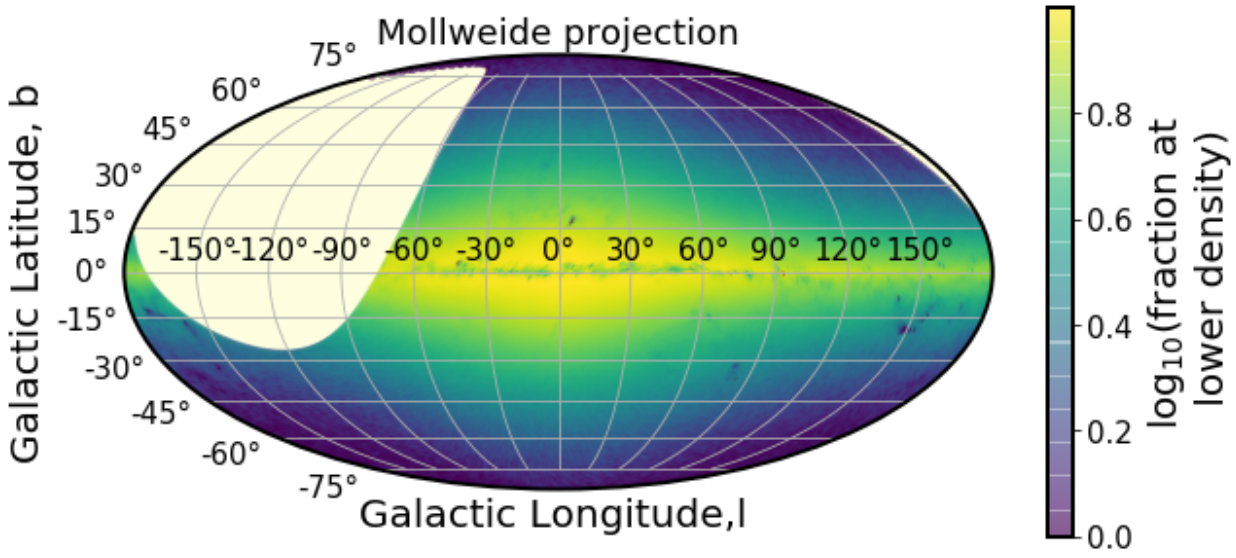

FIGURE 1: MAF healpixels plotted in galactic coordinates in Mollweide projection. The brightest regions correspond to highest stellar densities. The missing part in the higher declination is the part of the sky above $\delta > 40°$, which is not observable from the southern location of Cerro Pachón.

To match the LSST single-visit depth, we select magnitude bins smaller than r=24.5. For each healpixel we calculate the number of pixels that have a higher stellar count. Since each healpixel has an equal area, the fraction of pixel number above a certain threshold corresponds to the fraction of sky area above given density limit. Fig. 2 illustrates how we define percentiles of stellar densities, so that eg. 'top 1%' density means that only 1 in 100 pixels has a higher density than a given pixel, and 'top 10%' means that '10 %' of pixels in the considered simulation of the sky.

[3] `https://www.lsst.org/scientists/simulations/maf`, and `https://github.com/lsst/sims_maf`
[4] `sims_maf/python/lsst/sims/maf/maps/createStarDensitymap.py`
[5] `http://healpix.sourceforge.net`

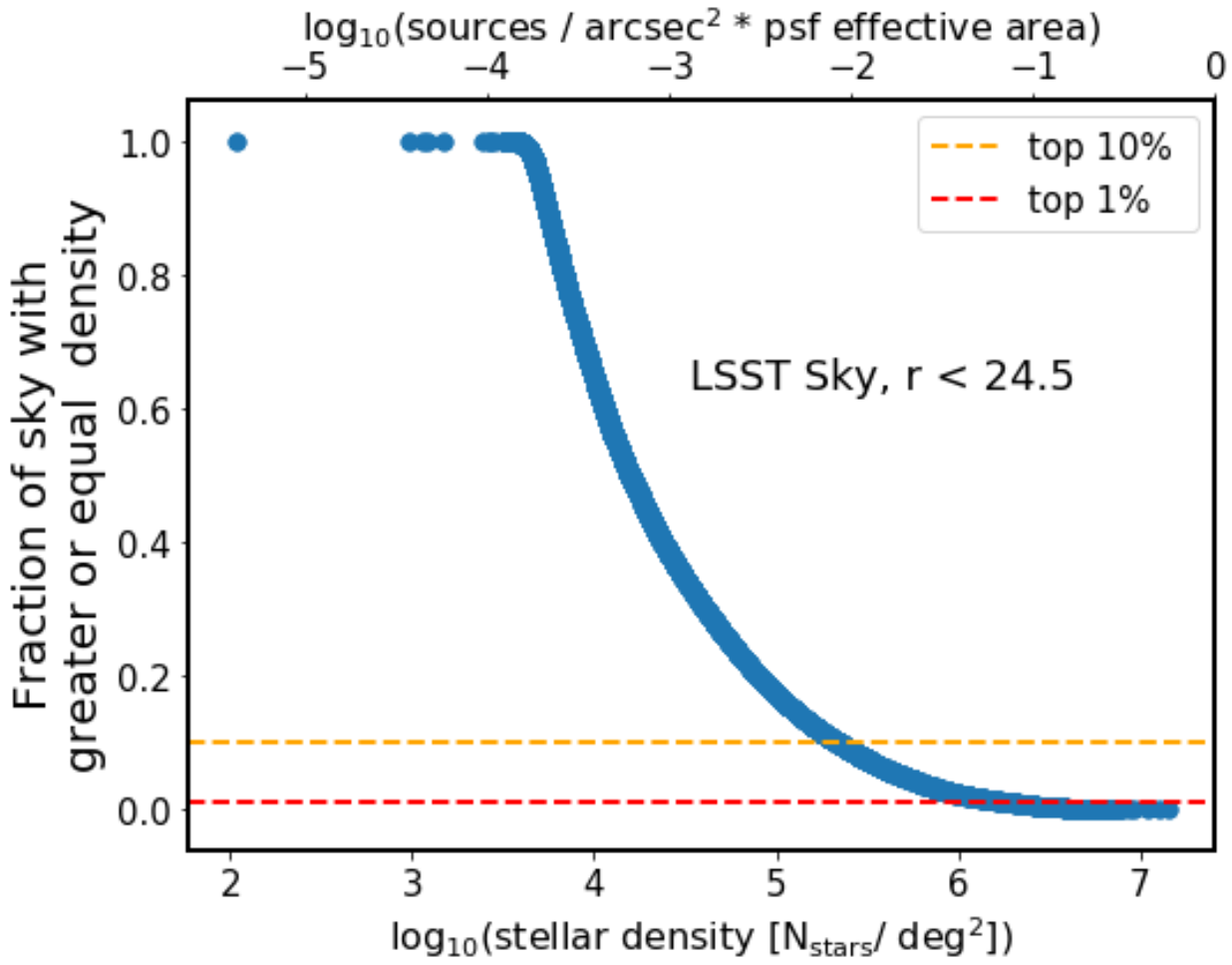

FIGURE 2: We order all healpixels in the MAF simulation of LSST sky in terms of stellar count per pixel. For each healpixel we calculate the number of pixels at greater or equal stellar count, which corresponds to the area of the sky at greater density. Normalizing that by the total number of pixels we obtain a fraction of the sky at greater or equal density, similar to the cumulative distribution. Horizontal dashed lines illustrate selecting pixels at 5% or 10% density.

Since this definition of density includes all pixels that are within 'top 20%', we take selection around the percentiles so that :

- top 1 % means fraction of sky with greater density is 0.01
- 5 % region means such that between 4% and 6%
- 20 % region includes 19% - 21%
- 50 % region includes 49% - 51%

We illustrate the location of pixels representative of these density brackets on the sky in Fig. 3.

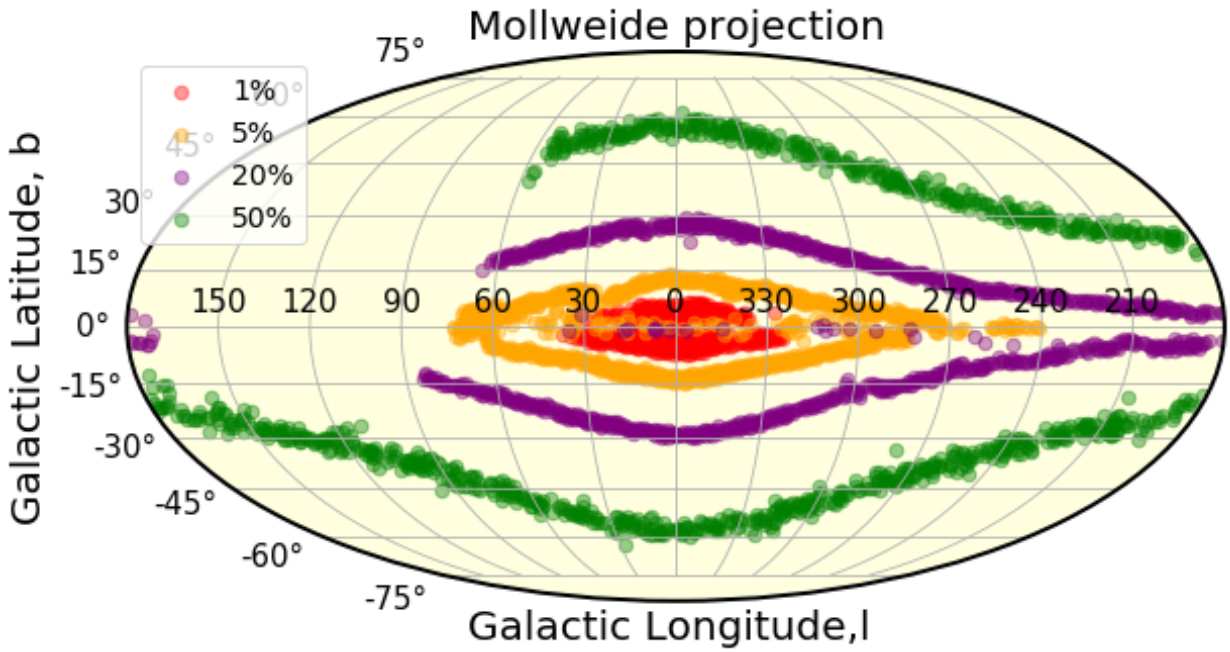

FIGURE 3: Illustration of location of regions representative of different relative density in cylindrical projection, galactic coordinates. The highest density regions are located close to the galactic bulge, and the decreasing density regions approximately trace isophotes of the Milky Way. The 20% regions close to the galactic equator correspond to high extinction regions that appear to have less counts due to interstellar dust.

3 DECam Plane Survey

To analyze the performance of the LSST Stack with real data, we used the Dark Energy Camera (DECam) imaging, taken as part of the DECam Plane Survey (DECAPS) [5], at the 4-m Cerro

Tololo Inter-American Observatory telescope (CTIO)[6]. On Fig. 4 we overlay the locations of all DECAPS fields on top the MAF map of the LSST sky. All DECAPS single-epoch images were processed with the DECAPS pipeline, resulting in single-epoch catalogs. The headers of all catalogs were assembled into the image database that contains information about single-visit exposure time, filter, time of observation, position, etc. It was used to select DECAPS fields with single-epoch depth similar to that of the single-visit depth of 30 sec LSST exposure. Thus we selected DECAPS fields with exposure between 90 and 125 sec, taken in u, g, r, or VR filter.

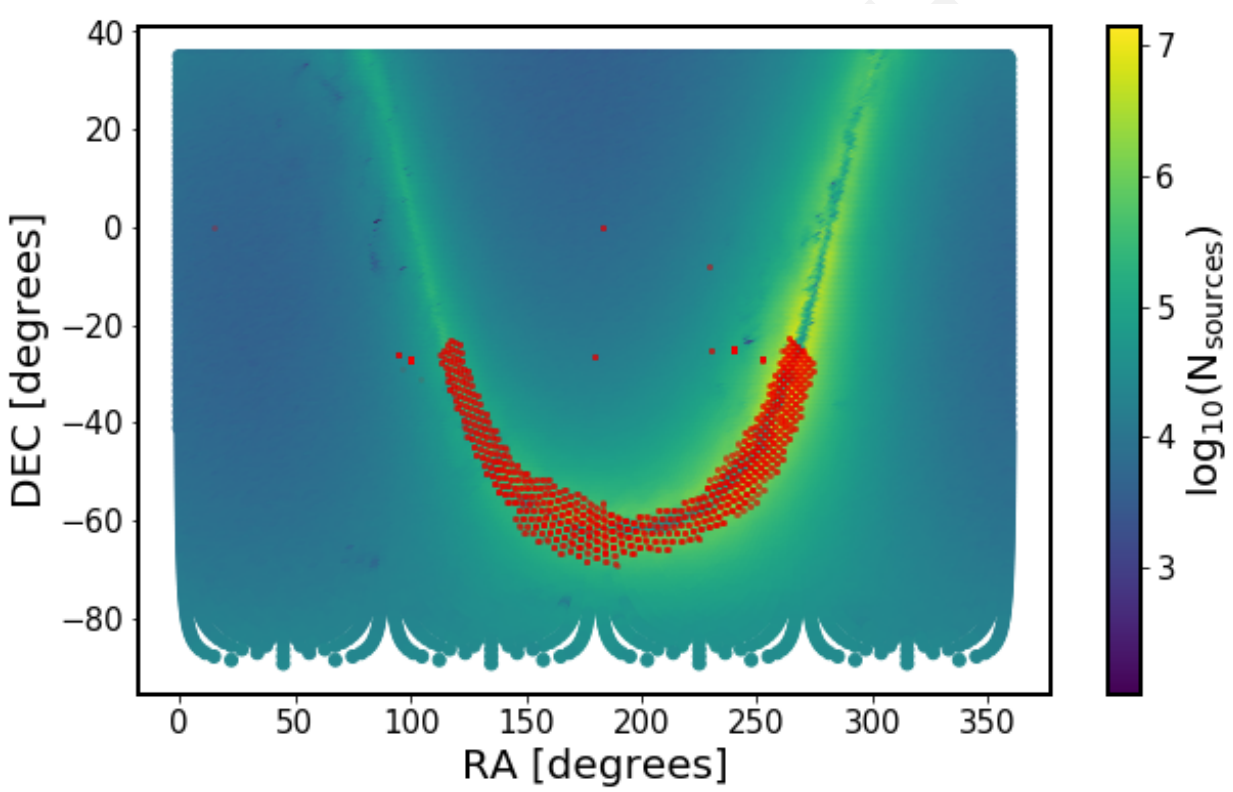

FIGURE 4: All DECAPS fields, overlaid on the map of healpixel stellar densities from MAF simulated sky. We matched the position of the center of each DECAPS field to the nearest healpixel to obtain an estimate of stellar density at each DECAPS field. In this way we selected DECAPS fields representative of various stellar densities (eg. 5%, 10%, 15%, as explained in Sec. 2).

We cross-matched the DECAPS image database with the stellar density information contained in MAF healpixels. Each DECAPS image plane is tiled by a mosaic of 62 CCDs (see Fig. 5). The size of each CCD element of the DECAm image plane mosaic is 2046x4094 pixels, with pixel scale of 0.27 arcsec / px , so that a single mosaic element covers an area of 0.047117 square °. A single DECam exposure is also called a visit, and with 62 mosaic elements the full field of

[6]see `http://www.ctio.noao.edu/noao/node/1033`

view 2.2°wide is several times bigger than the full moon. This makes it comparable to the LSST 3.5°wide field of view. Using the coordinates of the center of each DECAPS field we found the nearest healpixel within 0.5°.

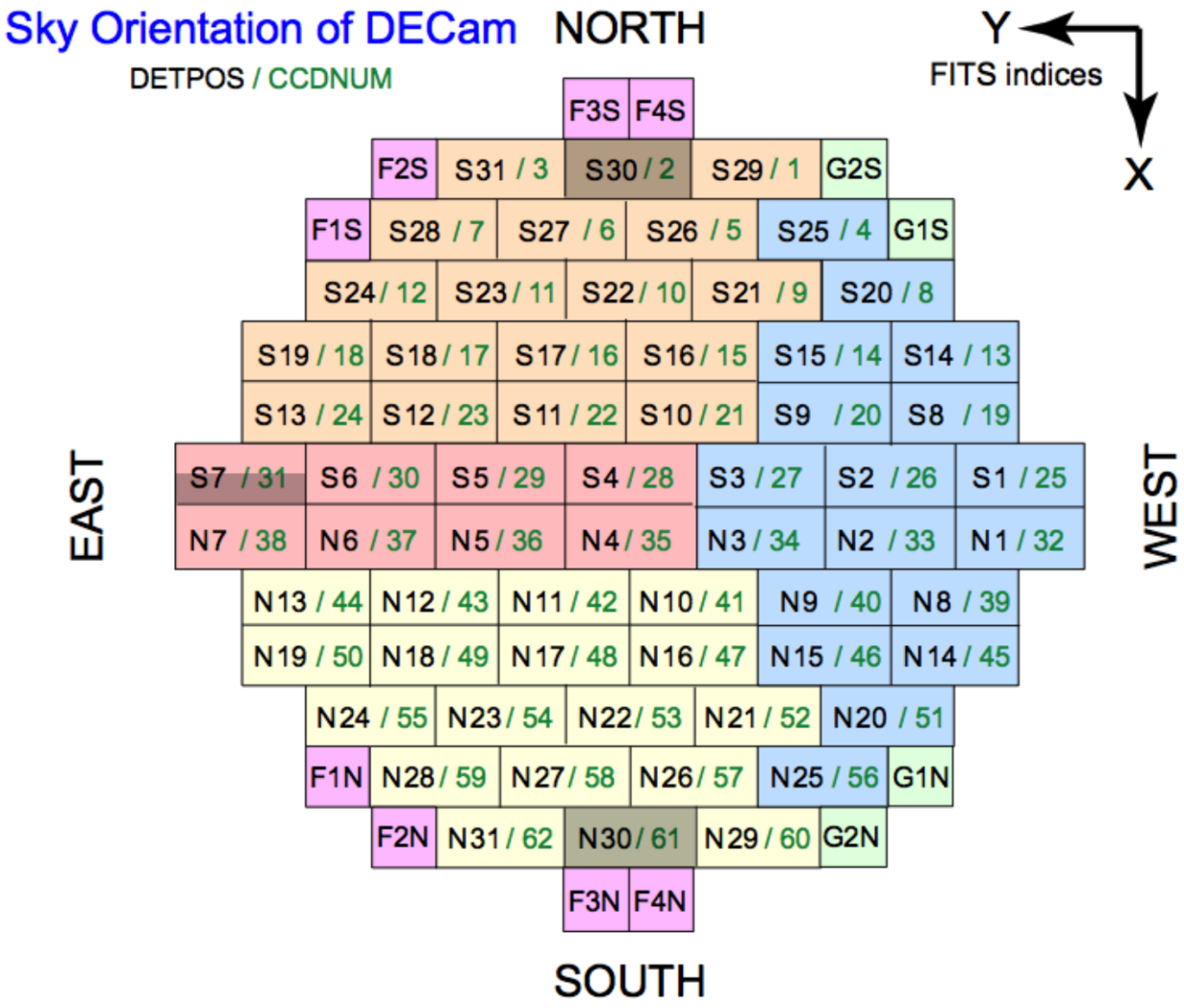

FIGURE 5: An illustration of the DECam CCD mosaic image plane, adapted from Fig.4-3 in NOAO Data Handbook [6], . The color corresponds to the one of the four sets of read-out electronics (orange,pink, blue,yellow), or the guiding (green) and focus (magenta) CCDS. The grey CCDs do not function properly. For this reason S30, S7, and N30 were excluded from the analysis.

4 LSST Processing of DECAPS data

The DECAPS calibrated imaging was processed with the LSST Science Pipelines installed on the LSST-dev machine installed at the NCSA. We specifically employed processCcd.py and the standard Stack configuration. Transferring the resulting source catalogs and calexp files over scp we analyzed the output on a laptop with jupyter notebooks.

To obtain independent order of magnitude comparison to MAF simulation, and LSST/DECAPS processing of DECam data, we also queried TRILEGAL simulation data, and processed the DECam images with DAOPhot - see Appendix A.

The big picture is to find how metrics that we develop behave as a function of source crowdedness. We consider completeness, and photometric accuracy.

4.1 Cleaning DECAPS catalog, comparison to LSST pixel mask

4.2 Cleaning LSST catalog

4.3 Completeness

4.4 Photometric accuracy

5 Conclusion and future work

5.1 LSST Processing of StarFast Simulated Sky

An independent way to further test the performance of the LSST Science Pipelines is to use the simulated sky images, where the true position and brightness of each source is known. This would put the measure of source detection completeness, photometric and astrometric precision on an absolute scale. We already tested a StarFast image simulator[7], and confirmed that it can successfully simulate a region of the sky seeded with known stellar population.

5.2 Other LSST-DECAPS tests: w-color

[7] https://dmtn-012.lsst.io

archive	l	b	TRILEGAL	MAF	DAO
c4d_140624_080728_ooi_r	13.70	-4.43	7,960,511	2,650,680	498,760
c4d_170428_094150_ooi_g	356.86	-3.90	39,852,793	4,587,804	375,980
c4d_170501_055757_ooi_g	356.26	5.05	16,352,821	2,659,968	285,630
c4d_170504_084722_ooi_g	4.26	5.15	15,586,874	2,833,740	561,795

TABLE 2: Source density comparison for 1% density level : TRILEGAL, DAO and MAF columns contain stellar counts from TRILEGAL simulation , DAOStarFinder based on DECam data, and MAF simulation, respectively. All counts are in stars per square degree.

archive	l	b	TRILEGAL	MAF	DAO
c4d_160316_065235_ooi_g	301.42	3.40	1,606,135	591,336	179,277
c4d_160825_231905_ooi_g	314.05	3.08	2,564,964	589,572	127,088
c4d_170429_035748_ooi_g	310.43	-4.02	1,870,414	807,156	327,483
tu1677011	4.48	8.70	2,530,163	810,144	509,093

TABLE 3: Source density comparison for 5% density level, all columns and units as in Table 2

A Appendix A: TRILEGAL and DAOPhot

A.1 DAOStarFinder source detection

Per each density regime, we performed source extraction with DAOStarFinder[8]. This tool uses a classic DAOFIND algorithm [7], and we used it to verify the plausibility of the MAF source densities using real data. We performed a straightforward DAOPhot source extraction setting the detection threshold at 5σ level, setting the detection threshold at 5σ.

A.2 TRILEGAL queries

For the same regions of the sky we also obtained TRILEGAL[9] simulation results, keeping r < 24.5 sources, with all other run settings as default.

A.3 Comparison of MAF, DAOStarFinder, and TRILEGAL counts

We used the number of sources per TRILEGAL output file, and scaled it to the degree level to compare with MAF and DAO. The results are shown in Tables 2, 3 , 4 , 5 for 1%,5%,20% and 50 % density levels.

[8] http://photutils.readthedocs.io/en/stable/photutils/detection.html
[9] http://stev.oapd.inaf.it/cgi-bin/trilegal

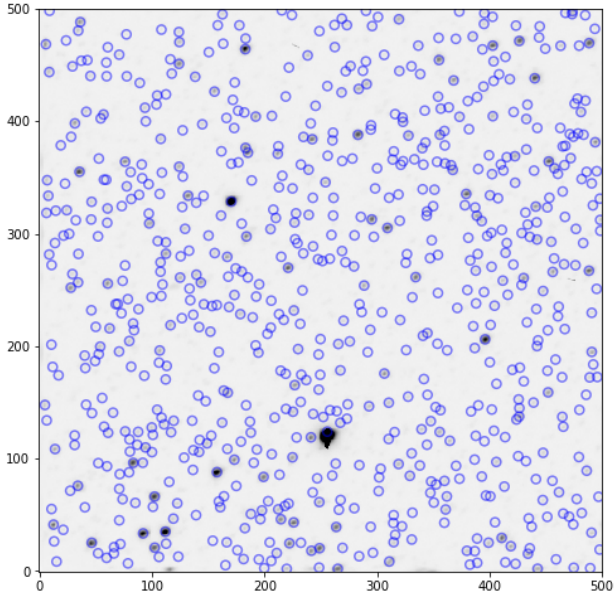

FIGURE 6: 500x500 pixels (135x135 arc-seconds) subregion of DECam field c4d_170504_084722_ooi_g, a top 1% density region. With DAOPhot threshold set at 5 σ, we detected 722 sources in this postage stamp miniature, corresponding to the area of 0.001406 sq degrees, which translates to 513,422 sources per square degree. At the same coordinates, MAF density is 2,833,740 sources per square degree, and TRILEGAL density is 15,586,874 sources per square degree.

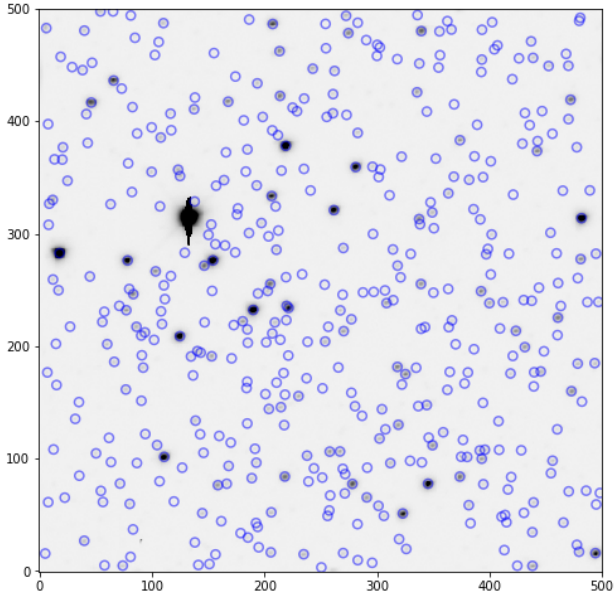

FIGURE 7: 500x500 pixels (135x135 arc-seconds) subregion of DECam field c4d_170429_035748_ooi_g, with 436 detected sources, in the 5 % density region. The same DAOPhot settings as Fig. 6. That many sources in an area of 0.001406 sq degrees, translates to 310,044 sources per square degree. At the same coordinates, MAF density is 807,156 sources per square degree, and TRILEGAL density is 1,870,414 sources per square degree.

archive	l	b	TRILEGAL	MAF	DAO
c4d_170122_055542_ooi_g	242.43	3.77	341,343	116,856	66,282
tu1661798	351.66	20.42	183,778	118,188	44,216
tu1668579	217.04	1.21	379,319	111,096	54,004
tu2187073	312.84	14.64	184,583	107,784	60,678

TABLE 4: Source density comparison for 20% density level, all columns and units as in Table 2

archive	l	b	TRILEGAL	MAF	DAO
c4d_150615_005257_ooi_g	344.39	41.67	27,633	21,024	12,904
c4d_160607_025052_ooi_g	2.92	41.68	29,607	20,052	13,371
c4d_160825_034122_ooi_g	345.83	1.28	18,364,268	20,268	91,177
tu2046406.fits.fz	220.89	-16.08	41,832	19,944	35,974

TABLE 5: Source density comparison for 50% density level, all columns and units as in Table 2

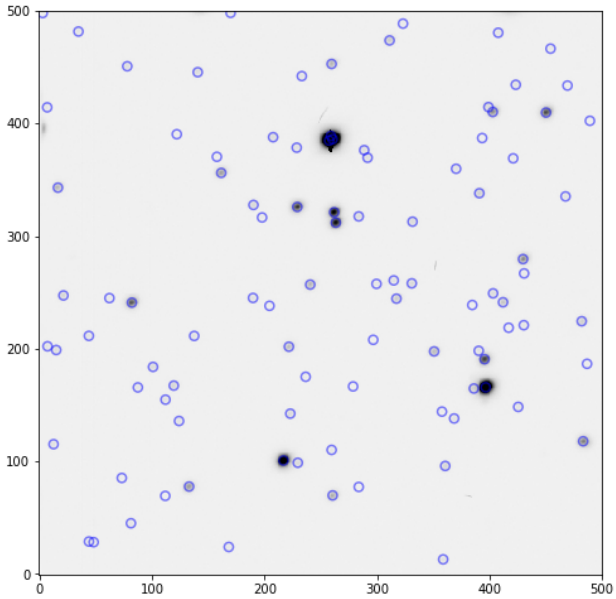

FIGURE 8: 500x500 pixels (135x135 arc-seconds) subregion of DECam field c4d_170122_055542_ooi_g, with 98 detected sources, in the 20 % density region. The same DAOPhot settings as Fig. 6. That many sources in an area of 0.001406 sq degrees, translates to 69,688 sources per square degree. At the same coordinates, MAF density is 116,856 sources per square degree, and TRILEGAL density is 341,343 sources per square degree.

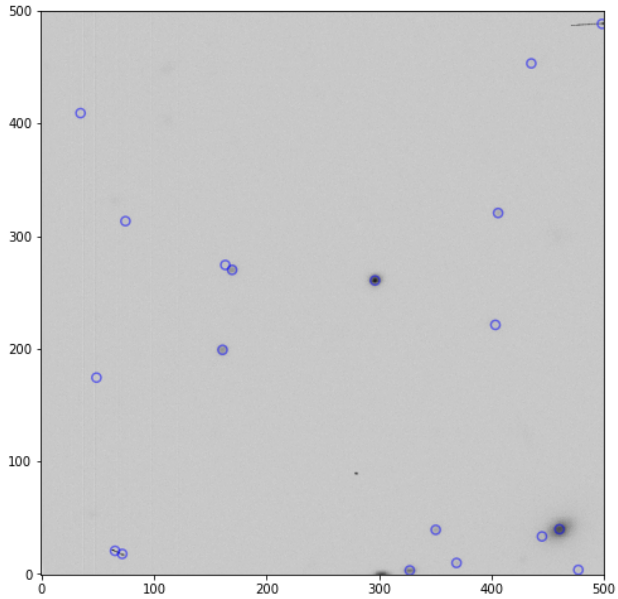

FIGURE 9: 500x500 pixels (135x135 arc-seconds) subregion of DECam field c4d_160607_025052_ooi_g, with 19 detected sources, in the 50 % density region. The same DAOPhot settings as Fig. 6. That many sources in an area of 0.001406 sq degrees, translates to 13,511 sources per square degree. At the same coordinates, MAF density is 20,052 per square degree, and TRILEGAL density is 29,607 sources per square degree.

References

[1] Bosch, J., et al. 2017, ArXiv e-prints

[2] Hogg, D. W. 2001, The Astronomical Journal, 121, 1207

[3] Narayan, G., et al. 2018, ArXiv e-prints

[4] Olsen, K. A. G., Blum, R. D., & Rigaut, F. 2003, AJ, 126, 452

[5] Schlafly, E. F., et al. 2017, ArXiv e-prints

[6] Shaw, R. A. 2015, NOAO Data Handbook

[7] Stetson, P. B. 1987, PASP, 99, 191